communications earth & environment
A Nature Portfolio journal

Article

https://doi.org/10.1038/s43247-026-03564-2

Decoding marine low cloud changes reveals more resilient climate feedbacks

Jinming Ge[1,7], Yize Li[1,7], Nan Peng[1], Jing Su[1], Chen Zhou[2], Jiajing Du[3], Xiaoyu Hu[4], Zeen Zhu[5], Jianping Huang[1] & Qiang Fu[6]

Marine low-level clouds' response to warming remains the largest uncertainty source in climate projections, limiting confidence in future warming estimates. We present a principal component-based method that integrates the physical processes associated with complex and indirect nonlinear covariations among multiple interdependent meteorological factors, providing a robust observationally constrained framework for reducing model biases. Using this framework, we find a smaller marine low-level cloud fraction reduction than direct model projections, particularly under the high CO_2 emission scenario. While models simulate a substantial future decrease in marine low-level cloud fraction during the 21st century, our results show marine low-level clouds reveal more moderate declines and even regional increases. The resulting global marine low-level clouds feedback under the high CO_2 emission scenario is 0.09 ± 0.09 $Wm^{-2}K^{-1}$, less uncertain than idealized abrupt CO_2 increase experiments estimates, suggesting that atmosphere-ocean adjustments buffer cloud responses and the climate system may be more resilient than previously thought.

Global climate change, driven by anthropogenic greenhouse gas emissions, has led to unequivocal surface warming[1]. Yet, the rate and magnitude of future warming remain highly uncertain, with equilibrium climate sensitivity in state-of-the-art models spanning 2.5–4.0 °C[2–4]. This persistent spread reflects difficulties in representing processes that strongly modulate Earth's top-of-atmosphere energy budget, foremost among these clouds, especially the marine low-level clouds (MLCs)[5]. Because of their vast coverage and high reflectivity, MLCs exert radiative effects comparable in magnitude to those of greenhouse gases with subtle shifts in their extent or other physical properties[6,7]. Observations suggest marine low cloud fraction (LCF) decreases with rising global temperatures, indicating a positive feedback that would amplify future warming[8–12]. However, most climate models either overestimate this reduction or show divergent responses across models[11,13]. Indeed, the Coupled Model Intercomparison Project (CMIP6) simulations show an even broader spread in climate sensitivity than their predecessors, underscoring the challenge of reliably representing low-cloud processes[11,14].

The difficulty arises because MLCs emerge from a complex interplay of boundary-layer processes and large-scale circulation, which current numerical models struggle to resolve[15,16]. A promising strategy is to link cloud variability to large-scale meteorological controlling factors that are generally better simulated than cloud themselves[17–22]. Previous approaches have attempted to establish relationships between cloud variability and specific meteorological factors using a linear Taylor expansions framework[23–25]. However, such methods are anchored to a baseline climate state over broad spatial scales and neglect the inherently nonlinear interactions between clouds and their governing factors[8]. This can lead to overfitting when too many predictors are included, or to incomplete representations when key variables are omitted[26–28]. Moreover, evolving climate spatial patterns, such as shifts in sea surface temperatures, can undermine the stability of these relationships[29]. Consequently, their effectiveness in capturing cloud-meteorology interactions, cloud variations, and their feedback on future climate change is substantially limited[6,30–32]. To address this challenge, we consider a key feature that the variability of meteorological factors governing MLC formation and evolution is markedly amplified under cloudy conditions relative to clear skies. This joint variability can be well represented by the leading principal component (PC1) derived from Principal Component Analysis (PCA), which integrates multiple atmospheric factors into a single, independent index. Although PCA is mathematically linear, PC1 encapsulates complex, indirectly nonlinear interactions among meteorological factors, filtering out unrelated noise and isolating processes most relevant to low cloud processes[33–35] (see

[1]Key Laboratory for Semi-Arid Climate Change of the Ministry of Education and College of Atmospheric Sciences, Lanzhou University, Lanzhou, China. [2]School of Atmospheric Sciences, Nanjing University, Nanjing, China. [3]Institute of Plateau Meteorology, China Meteorological Administration, Chengdu, China. [4]Intelligent Consultation and Artificial Intelligence Weather Forecasting Laboratory, Peking University Chongqing Big Data Research Institute, Chongqing, China. [5]Environmental and Climate Sciences Department, Brookhaven National Laboratory, Upton, NY, USA. [6]Department of Atmospheric Sciences and Climate Science, University of Washington, Seattle, WA, USA. [7]These authors contributed equally: Jinming Ge, Yize Li. e-mail: hjp@lzu.edu.cn

"Methods"). In earlier regional studies, by combining cloud radar observations with ERA5 reanalysis, we have demonstrated that PC1 provides a robust representation of low-cloud evolution at both the Semi-Arid Climate and Environment Observatory of Lanzhou University[32,35] and the Southern Great Plains atmospheric observatory[34]. While these validations were conducted over land, the present study extends this framework to 40°S−40°N marine regions by using satellite-based (CERES) cloud observations together with reanalysis data, enabling an examination of its applicability to MLCs.

In this study, we extend the PCA framework to the near-global scale to link MLCs with large-scale meteorological drivers, providing observationally grounded constraints that reduce uncertainty in future cloud variability and their feedbacks. Specifically, we establish the link between CERES-observed cloud fraction and the leading principal component from ERA5 reanalysis ($PC1_{ERA5}$) over oceanic regions (40°S−40°N), and project future changes in PC1 using CMIP6 simulations ($PC1_{CMIP6}$). This allows us to constrain MLC responses and quantify their radiative feedbacks under both low- (Shared Socioeconomic Pathway 126, SSP126) and high-carbon (SSP585) emission scenarios. Our results show that PC1 effectively captures both the spatial organization of MLCs and their sensitivity to meteorological drivers. Crucially, PC1-based projections indicate that future MLC feedbacks are less extreme than many direct model outputs suggest, narrowing the upper tail of climate sensitivity, particularly under high-carbon emission scenarios. This study highlights biases in state-of-the-art model simulations of MLCs, while providing a process-based, observationally grounded framework for more reliable projections of future cloud variations, feedbacks, and climate change.

Results

First principal component controlling low-level cloud fraction

We selected four key large-scale meteorological factors from ERA5: sea surface temperature (SST), vertical velocity (ω_{700}), and relative humidity at 700 hPa (RH_{700}), and lower-tropospheric stability (LTS) that jointly govern the moisture supply, atmospheric dynamics, and thermal structure influencing MLCs evolution[8,28,31,36] (Supplementary Note 1 and Fig. S1). Applying PCA to these variables, we obtained the $PC1_{ERA5}$, which represents the leading direction of joint variability among four meteorological factors regulating the maintenance and dissipation of MLCs (Fig. 1B). Although PCA is inherently a linear method, the PC1 effectively captures the combined influence of nonlinear dynamical and thermodynamical processes acting across multiple meteorological factors. We further tested the sensitivity of PC1 and found that the statistical relationship between PC1 and CERES-observed LCF remains stable when meteorological predictors are added or removed. This indicates that the PC1-based framework partially alleviates the sensitivity of low cloud feedback estimates to the choice of controlling factors. Moreover, the PC1 framework is well-suited for application to high-resolution observational and model datasets, maintaining statistical robustness while maximizing the representation of spatial heterogeneity in low cloud feedbacks across different ocean basins and dynamical regimes (Supplementary Note 2 and Figs. S4–S6).

Figure 1A illustrates the distribution of LCF observed by CERES, closely reflecting the spatial pattern of $PC1_{ERA5}$ (Fig. 1B). The strong spatial negative correlation coefficient of −0.86 between $PC1_{ERA5}$ and LCF surpasses those obtained with individual meteorological variables (Supplementary Note 1 and Fig. S1). CERES-MODIS synthesis product reveals that MLCs are predominantly distributed over the subtropical eastern Pacific and Atlantic Ocean basins, especially along the western coasts of continents, the trade wind zones in the tropics, the Southern Ocean, and other Mid-latitude regions, driven by distinct atmospheric and oceanic processes[6,9]. The regions with large negative values of $PC1_{ERA5}$ closely correspond to areas characterized by cold SST, strong descending motion, and a dry, stable upper atmospheric layer above cloud top, which are conducive to the formation of low clouds. In contrast, large positive $PC1_{ERA5}$ values are linked to warm SST, intense ascending motion, high humidity, and an unstable atmosphere (Supplementary Note 1 and Fig. S2), primarily in equatorial convergence zones and tropical west Pacific and Indian Oceans (Fig. 1B), where converging warm, moist air masses promote the widespread deep convective clouds[16,30,37]. In addition, we examine the correlation coefficients between the time series of marine LCF and $PC1_{ERA5}$ at each grid. The results show that, after deseasonalized and detrended, the relationship between $PC1_{ERA5}$ and LCF exhibits certain regional differences, which primarily

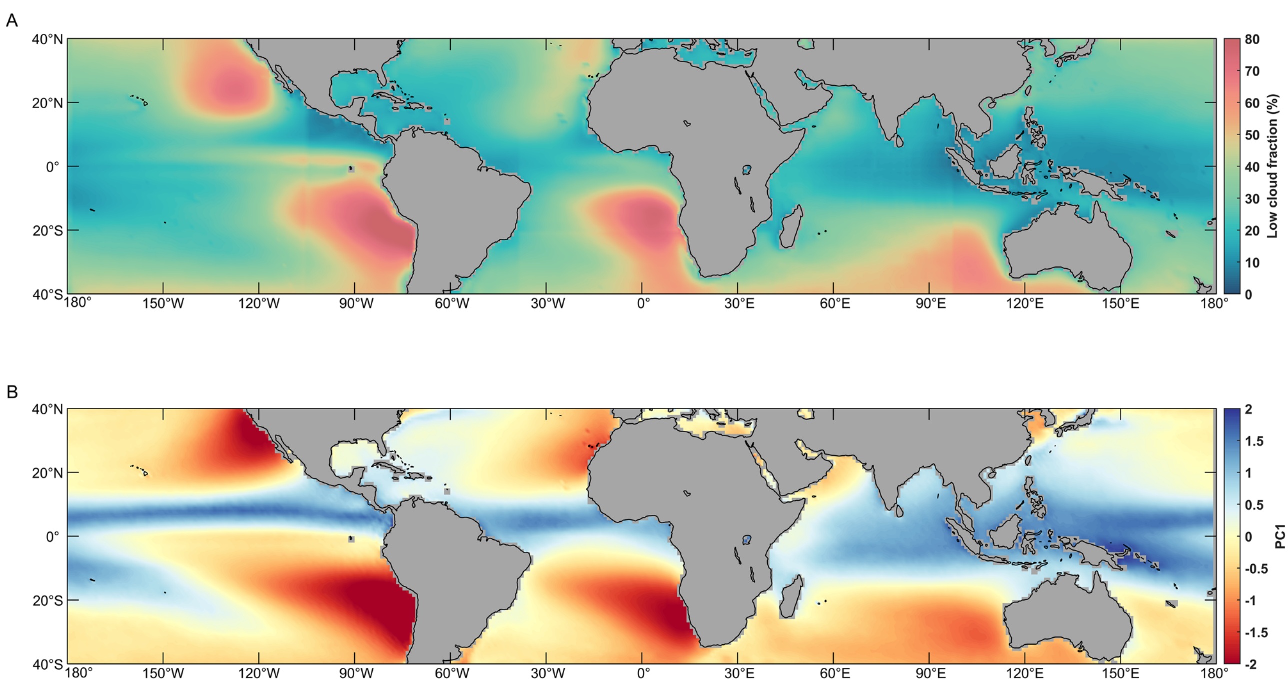

Fig. 1 | The spatial distributions of marine low cloud fraction between 40°N and 40°S and the first principal component (PC1) of four key meteorological variables, including sea surface temperature, relative humidity at 700 hPa, vertical velocity at 700 hPa, and the lower-tropospheric stability, averaged over 2010–2019. A Low cloud fraction observed from CERES. **B** PC1 derived from ERA5. The spatial correlation coefficient between (**A**) and (**B**) is −0.86.

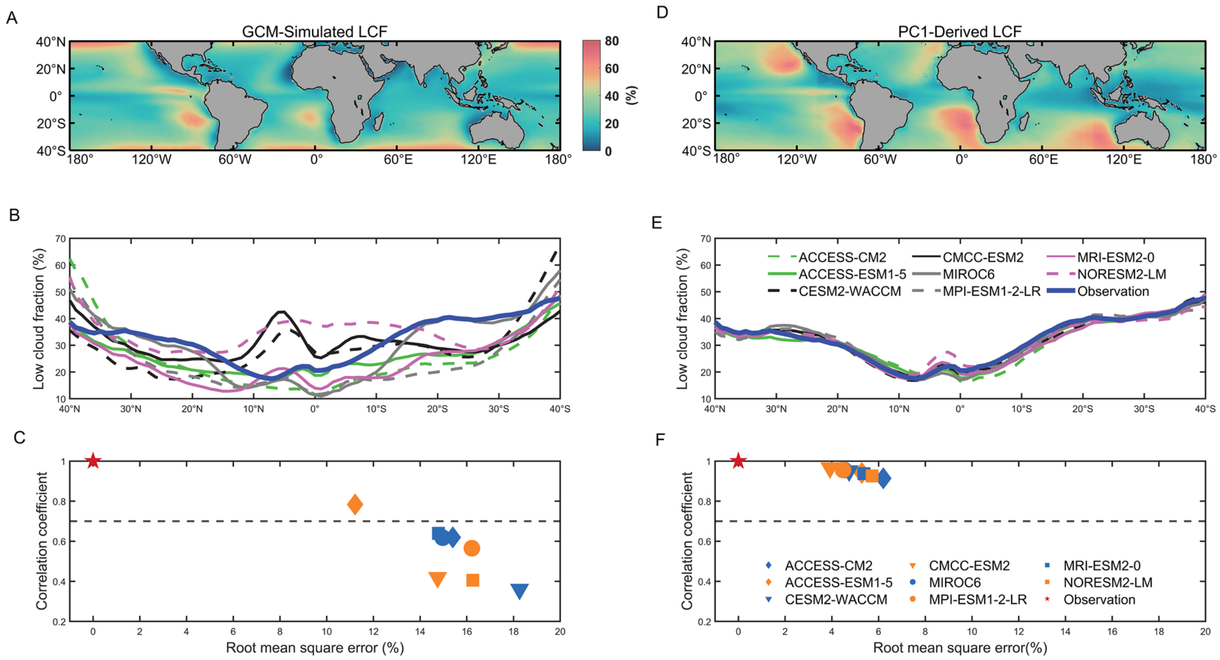

Fig. 2 | GCM-simulated low cloud fraction (LCF) (left column) and $PC1_{CMIP6}$-derived LCF (right column) for the historical period 2010–2014, along with evaluations against CERES observations. **A** Spatial distribution of multi-model mean LCF directly from simulations. **B** Latitudinal distribution of zonal-mean LCF from individual models compared to observations. **C** Spatial pattern correlation and root mean square errors between each model's simulated LCF and observations. **D–F** same as (**A–C**) but for $PC1_{CMIP6}$-derived LCF.

reflect variations in the physical mechanisms controlling low clouds across regions. However, from an overall perspective based on the original data, the consistently high correlation across most ocean regions, even over the Intertropical Convergence Zone and surrounding regions characterized by extensive high-cloud, the correlation coefficient remains as high as approximately 0.8 (Supplementary Note 1 and Fig. S3). This strong correspondence underscores PC1 as a robust indicator of both the spatial and temporal variations of MLCs across oceanic regions.

Improving low cloud fraction estimates from models through PC1 analysis

We applied PCA to the same four meteorological controlling variables from eight CMIP6 models during the historical period 2010–2014 to derive $PC1_{CMIP6}$ (details provided in "Methods" and Supplementary Table S1). We performed a linear regression at each grid point between the CERES-observed LCF and $PC1_{ERA5}$ using monthly data from 2010 to 2019 to obtain the corresponding regression coefficients. The multi-model mean $PC1_{CMIP6}$ derived from the eight CMIP6 models was then applied to this observationally constrained regression to estimate PC1-based LCF (LCF_{PC1}) from the $PC1_{CMIP6}$ values. If LCF_{PC1} aligns more closely with observations than direct simulations, the PC1-constrained framework can be a more reliable basis for projecting future LCF changes and associated low cloud feedbacks. Fig. 2 (left column) depicts the multi-model mean distribution of simulated LCF according to Eq.(3) in method (Fig. 2A), the latitudinal dependences of zonal-mean LCF from individual models compared to CERES observations (Fig. 2B), and the spatial pattern correlation and root mean square errors between each model's simulated LCF and observations (Fig. 2C). The corresponding PC1-derived results are shown in the right column. All datasets were re-gridded into a 1° × 1°resolution two-dimensional cubic interpolation for consistency.

A comparison of Figs. 1A, 2A reveals that, while the models capture the overall spatial pattern of oceanic LCF, they underestimate LCF in low-cloud-dominated regions, reaching approximately 20%, particularly along the western coasts of continents, a well-documented deficiency known as the "too few too bright bias"[11,38]. Similar biases are evident in the LCF distributions from individual models (Supplementary Note 3 and Fig. S7 left and right columns). The zonal-mean LCF in Fig. 2B further highlights large discrepancies between direct model simulations and observations, with differences up to 40%. In contrast, the spatial pattern of simulated PC1 aligns closely with that of $PC1_{ERA5}$ (Supplementary Note 3 and Fig. S7 middle column versus Fig. 1B). The multi-model mean LCF pattern derived from $PC1_{CMIP6}$ (Fig. 2D) shows strong agreement with CERES observations (Fig. 1A), and the differences between zonal-mean LCF_{PC1} from individual models relative to CERES observations are substantially smaller, less than about 6% (Fig. 2E).

To quantitatively assess both the directly simulated LCF and model-derived LCF_{PC1} against observations, we conducted spatial correlation and root mean square error (RMSE) analysis. Correlation coefficients between model-simulated LCF and observations range from 0.3 to 0.6, with only one model achieving 0.7, while RMSE values fall between 11% and 19% (Fig. 2C). In contrast, LCF_{PC1} shows much better agreement with observations, with all correlation coefficients exceeding 0.9 and RMSE values ranging between 3 and 7% (Fig. 2F). These results highlight the effectiveness of the PC1-based approach in representing MLCs, as it substantially reduces the inter-model spread and greatly narrows the gap between model estimates and observations. Consequently, using PC1 to derive LCF offers a promising strategy to minimize uncertainties in estimates of MLC feedback compared to direct model simulations[32].

Projecting the future trend of low cloud fraction

We performed PCA separately for all eight CMIP6 models, obtaining a $PC1_{CMIP6}$ time series for each model. The PC1 from the eight models was then averaged to produce a multi-model mean $PC1_{CMIP6}$. The consistent $PC1_{CMIP6}$ patterns and corresponding LCF_{PC1} fields across all eight climate models, which closely match $PC1_{ERA5}$ and the observed LCF distribution, respectively, provide a reliable basis for inferring future LCF trends under global warming scenarios. Figure 3 compares projected LCF changes derived from $PC1_{CMIP6}$ with those directly simulated by CMIP6 models under both low- and high-carbon emission scenarios. Following the heuristic framework suggested by ref. 8, future LCF_{PC1} changes are estimated by

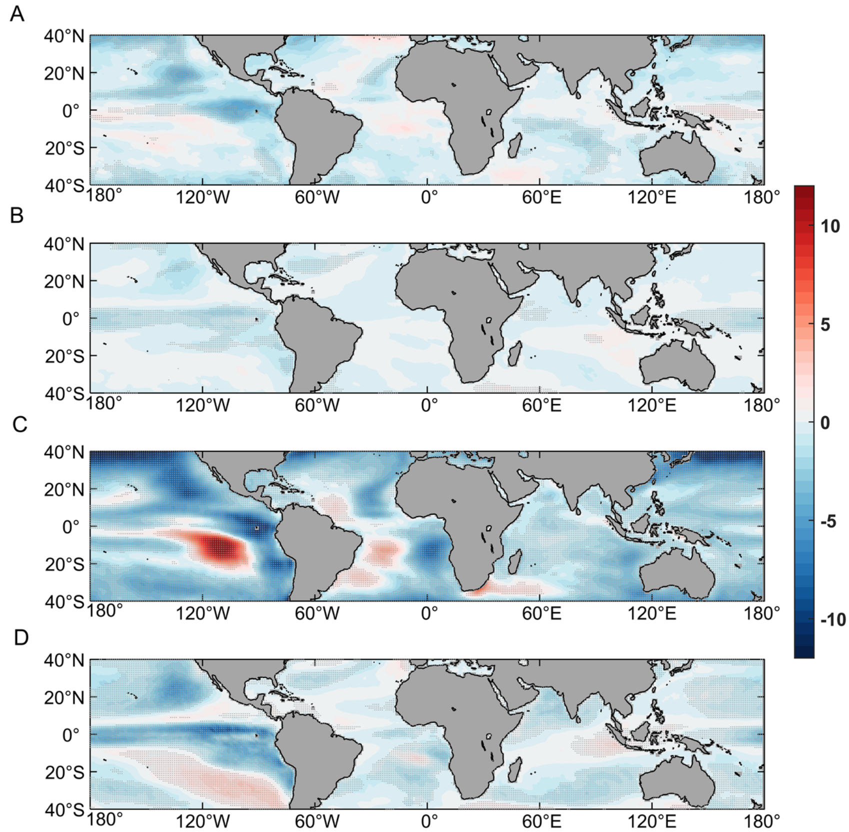

Fig. 3 | Predicted trends in low cloud fraction (LCF) from multi-model mean simulation for the period 2020 to 2100. A LCF trend directly from the model simulation under SSP126. **B** LCF trend derived from PC1 under SSP126. **C, D** Same as (**A**, **B**), but for SSP585. Gray dots indicate regions where the trends are statistically significant at the 95% significance level.

combining two components: (1) the sensitivity of LCF to PC1, derived from deseasonalized and detrended monthly CERES LCF and ERA5 PC1 data at each grid point over 2010-2019, if we do not use detrended data, then common long-term forcing (e.g., SST increase due to global warming) would introduce spurious correlations between LCF and PC1, causing the regression coefficients to mix climate trends with short-term physical responses and thereby bias the sensitivity estimates. In that case, the regression would reflect more the “co-variation over time” rather than the true cloud response to meteorological perturbations. And (2) the change in $PC1_{CMIP6}$ between the early (2020–2029) and late (2091–2100) decades, representing its simulated response to global warming.

Under the SSP126 scenario, the near-global patterns of LCF trends are relatively weak in both direct CMIP6 simulations and the $PC1_{CMIP6}$-derived estimates (Fig. 3A, B). However, the direct model simulations show a somewhat greater reduction in LCF over the eastern equatorial Pacific and along the western coasts of North and South America compared to the $PC1_{CMIP6}$-derived estimates. The decrease in MLCs is primarily attributed to the increased SST, which enhances convection and, in turn, decreases the stability of the lower atmosphere and increases the entrainment of dry air from the upper atmosphere, ultimately resulting in a reduction in LCF (Supplementary Note 4 and Fig. S8). The direct CMIP6 simulations also simulate slight increases over the equatorial Pacific, Atlantic, and Southern Oceans, but these changes are generally insignificant outside the equatorial region. Under the SSP585 scenario, the LCF change from direct model simulations diverge reaching up to about 10% from the $PC1_{CMIP6}$-derived estimates (Fig. 3C, D). Direct model simulations project a substantial decrease in LCF across most ocean regions, with especially pronounced reductions of about 10% along the western coasts of the Americas and Africa[39,40]. This pattern closely follows the distribution of changes in near-surface relative humidity, highlighting the role of this variable in current model low cloud parameterization (Fig. S9E). In contrast, LCF is notably enhanced in the eastern tropical South Pacific near 110°W, increases by approximately 6% along the eastern coast of South America, and in the Indian Ocean near the southern tip of Africa (Fig. 3C). The LCF variations derived from $PC1_{CMIP6}$ show a much smaller decline (Fig. 3D). They also indicate increases across a broad band stretching from the tropical South Pacific near 160°W to the Southern Ocean off the western coast of South America[31,39] (Fig. 3D). This increased LCF reflects strong ocean-atmosphere interactions, where enhanced southeast trade winds drive cold upwelling currents that cool the surface, stabilize the lower atmosphere, and favor low cloud formation (Supplementary Note 4 and Fig. S9D, F). The discrepancies between directly simulated and PC1-derived LCFs suggest that models may not fully capture the impact of key atmospheric dynamics, such as subsidence and boundary layer mixing, on MLCs.

Our analysis shows that changes in LCF under the SSP585 scenario are up to about 8% greater than those under the SSP126 scenario, regardless of whether they are directly simulated by climate models or derived based on meteorological conditions. Our conclusions are consistent with previous work[41], showing that some climate models tend to overestimate cloud feedback due to an excessive response in LCF. Particularly, the discrepancies between LCF trends from direct model simulations and those derived from $PC1_{CMIP6}$ highlight the complexity of projecting low cloud responses under SSP585 scenarios. These differences suggest that the actual reduction in low clouds may be less pronounced than indicated by current model simulations. In fact, a broad region may even experience an increase in LCF, as is the case for stratocumulus clouds when the SST pattern effect is considered. This implies that current models could be overestimating the positive feedback effect associated with low clouds[15,28].

Physically, the smaller LCF reduction indicated by the PC1-based approach reflects its improved representation of the large-scale ocean-atmosphere coupling processes that regulate marine low clouds. By integrating the covariation among SST, ω_{700}, LTS, and RH_{700}, PC1 captures the combined nonlinear environmental conditions favoring MLCs persistence, including surface cooling, boundary-layer stability, and modulation by large-scale subsidence. In contrast, some CMIP6 models may not fully resolve these coupled dynamical and thermodynamic constraints,

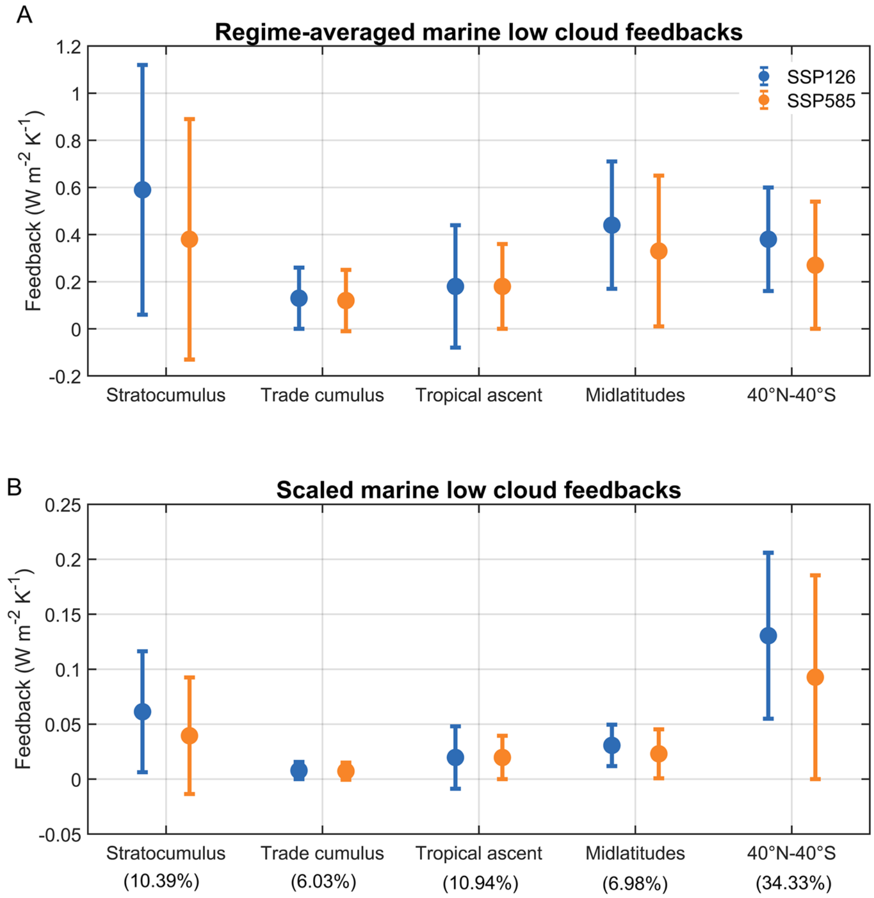

Fig. 4 | Marine low cloud feedbacks for four oceanic regimes and the whole regional average, estimated using the multi-model mean projections of PC1 combined with an observationally constrained radiative kernel. Error bars indicate 90% confidence intervals. **A** Regime-averaged low cloud feedback. **B** Global-mean feedback scaled by the fractional areas of each regime.

particularly boundary-layer mixing, subsidence strength, and its coupling with SST patterns, leading to a tendency to simulate a stronger LCF. Consequently, the PC1-based diagnostic provides a more observation-constrained and physically conservative estimate of future low cloud changes.

Constraining low cloud feedback

The cloud radiative effects of MLCs, defined as the changes in top-of-atmosphere radiative flux induced by MLCs, are primarily governed by their LCF, which exhibits a strong coupling with PC1. This strong linkage suggests that variations in cloud radiative effects of MLCs can be effectively inferred from changes in PC1. To estimate MLC radiative feedbacks, we combine the sensitivity of MLCs' radiative effects to PC1 (i.e., radiative kernel) with the projected response of $PC1_{CMIP6}$ to global temperature changes, as outlined in the previous section. To minimize contamination from other cloud types, we focus on regions predominantly occupied by MLCs. MLC's radiative effects were determined utilizing CERES data for the 2010–2019 period. After removing seasonality and long-term trends, ensuring that the derived sensitivity reflects the local, fast MLCs radiative effects response to meteorological perturbations under a fixed climate background. We regressed monthly anomalies of CERES-derived MLCs radiative effects against $PC1_{ERA5}$ anomalies to derive the radiative kernel at each grid point. These kernels were then multiplied by the projected changes in $PC1_{CMIP6}$ under different emission scenarios, yielding the spatial distribution of MLC radiative feedback[31,32,42,43] (Supplementary Note 5 and Fig. S10).

For a more nuanced understanding of how different low cloud types respond to climate forcing and to facilitate direct comparisons with previous studies on MLC feedback, we categorize oceanic regions between 40°S–40°N into four distinct regimes—Stratocumulus, Trade Cumulus, Tropical Ascent, and Mid-latitude—based on thresholds of ω_{700} and estimated inversion strength (EIS)[30,31], derived from a decade of ERA5 reanalysis data in Fig. 4. Our cloud type decomposition of low-cloud feedback reveals cloud type contrasts in both magnitude and scenario dependence. Stratocumulus decks along the eastern subtropical oceans exhibit the strongest positive feedback, reaching 0.59 ± 0.53 Wm^{-2}K^{-1} under SSP126 and 0.38 ± 0.51 W m^{-2}K^{-1} under SSP585, followed by the mid-latitude oceans (0.44 ± 0.27 vs. 0.33 ± 0.32 Wm^{-2}K^{-1}). In contrast, the trade cumulus (0.13 ± 0.13 vs. 0.12 ± 0.13 Wm^{-2}K^{-1}) and tropical ascendant regions (0.18 ± 0.26 vs. 0.18 ± 0.18 Wm^{-2}K^{-1} in both scenarios) contribute only about one-third of the stratocumulus and mid-latitude values (Fig. 4A). These values are comparable to the observationally constrained estimates of ref. 41 who reported an observationally constrained radiative feedback of approximately 0.44 W m^{-2}K^{-1} for stratocumulus and 0.12 W m^{-2}K^{-1} for cumulus clouds, which is comparable in magnitude to the stratocumulus feedback obtained here under SSP126 and indicates that our estimates fall within the range of previous observational constraints. These results reinforce the dominant role of stratocumulus and mid-latitude low clouds in setting the global feedback strength, while the relatively weak responses of trade cumulus and tropical ascent regions underscore their limited impacts on the large-scale radiative budget. Considering the proportion of global area occupied by each cloud regime, we scale these regional values to the global domain and compute the average in Fig. 4B, yielding small MLC feedbacks of 0.13 ± 0.08 Wm^{-2}K^{-1} for SSP126 and 0.09 ± 0.09 Wm^{-2}K^{-1} for SSP585. Stratocumulus contributes the largest portion, approximately 0.05 W m^{-2}K^{-1}, while trade cumulus contributes only 0.01 Wm^{-2}K^{-1}. Among previous observationally constrained studies, ref. 44 estimated a low-cloud radiative feedback of 0.25 ± 0.18 W m^{-2}K^{-1} over the tropics, ref. 41 reported a value of 0.56 ± 0.15 W m^{-2}K^{-1}, and ref. 31 obtained a global low-cloud feedback of 0.19 ± 0.12 W m^{-2}K^{-1}. Compared with these studies, the low-cloud feedback estimated here is smaller in magnitude but remains consistent in terms of order of magnitude.

Compared to earlier analyses based on abrupt CO_2 doubling experiments[3,31,43,44], our MLC feedback values under emission scenarios are the smallest with less uncertainty to date. This indicates that low clouds respond less strongly in the more realistic SSP scenarios than in the idealized abrupt CO_2 doubling case. It implies that existing models could be overestimating the MLC radiative feedback, potentially leading to a higher climate sensitivity and enhanced warming projections. This also means that, as climate change progresses gradually, the atmosphere and ocean can adjust in ways that moderate the immediate cloud response. The reduced low-cloud feedbacks indicate that both the magnitude and uncertainty of warming driven by low-cloud feedback may be smaller than previously anticipated, pointing to a more resilient climate system than originally expected.

Discussion

By introducing a principal component-based framework that links MLCs to large-scale meteorological controls across carbon emission scenarios, this study advances an important step forward in understanding and constraining cloud feedback. The reconstruction of LCF from PC1 demonstrates far closer agreement with CERES observations than direct CMIP6 simulations, underscoring the potential of this approach to reduce long-standing uncertainties in projecting cloud climate interactions. This methodological improvement provides a more physically grounded pathway for interpreting future MLC changes and their radiative effects.

Our results reveal that MLC responses to warming are neither spatially uniform nor linearly related to carbon emissions. MLC changes induce positive radiative feedback under both SSP126 and SSP585, but the feedback strength is weaker under SSP585 than under SSP126. Notably, the largest reductions in feedback sensitivity occur in stratocumulus regions of the equatorial eastern Pacific and along the subtropical eastern ocean basins, where feedbacks become weaker than CMIP6 simulations suggest. Trade cumulus and tropical ascent regimes exhibit more moderate declines, and in some regions, even slight increases in LCF, diverging sharply from the widespread decreases projected by the eight models examined here. These regime-dependent differences arise mainly from the different responses and combined effects of meteorological drivers across cloud regimes, highlighting the importance of treating MLC variability within a physically constrained framework. At the global scale, the PC1-based estimate of MLC feedback is 0.09 ± 0.09 W m^{-2}K^{-1} under SSP585, which is smaller in magnitude and less uncertain than estimates derived from CO_2-doubling experiments. Among which, ref. 44 reported a MLCs radiative feedback of 0.25 ± 0.18 W m^{-2}K^{-1}, while ref. 31 obtained a value of 0.19 ± 0.12 W m^{-2}K^{-1} from abrupt CO_2-doubling experiments, and ref. 41 reported a value of 0.56 ± 0.15 W m^{-2}K^{-1}. This finding suggests that Earth's climate sensitivity to emissions may be less extreme than implied by current model projections. However, the lower sensitivity of clouds does not offset the rapid rise in surface temperatures under SSP585 scenarios. Even with weaker cloud feedback, accelerated warming under SSP585 leads to a more uniform and globally pervasive radiative impact, emphasizing that no region remains insulated from climate change.

These insights carry two major implications. First, they call into question the degree to which CMIP6 models overestimate MLC loss and associated positive feedback, underscoring the value of physically constrained approaches in future model evaluation. Second, they reaffirm that aggressive emission reductions remain the most effective means to limit dangerous warming. While our results, consistent with previous observationally constrained studies[41], point to a climate system that may be somewhat more resilient than suggested by some model-based projections, unchecked emissions still overwhelm this resilience, with severe consequences for weather extremes, sea level rise, and ecosystem stability. Policymakers can leverage these refined projections to develop targeted mitigation strategies and prioritize regions most vulnerable to the cascading effects of warming-induced cloud feedbacks. Without obvious emission reductions, we risk accelerating global warming, leaving fewer regions untouched.

There are still some limitations to this study. Firstly, an implicit assumption of this study is that the sensitivity of LCF to the integrated meteorological controlling factor PC1 ($\frac{\partial LCF}{\partial PC1}$), derived from the historical period (2010–2019), remains approximately constant under future warming scenarios. This assumption is based on the fact that PC1 represents the impact of coordinated variations among multiple key large-scale meteorological factors on MLCs evolution over near-global scale oceans. Previous studies have shown that low clouds exhibit relatively robust statistical relationships with these variables[7,9,43]. However, continued warming may induce systematic changes in boundary-layer structure and cloud circulation coupling, leading to a change in the dependence of low cloud sensitivity. Therefore, the assumption of a time-invariant $\frac{\partial LCF}{\partial PC1}$ introduces uncertainty and constitutes an important limitation of the present approach. Future work combining longer observational records and model experiments across different climate states is needed to further evaluate the stability of this sensitivity relationship. Secondly, the framework in this study emphasizes the dominant large-scale meteorological controls on LCF distributions through the construction of PC1. We also note, however, that aerosols acting as cloud condensation nuclei can modulate cloud microphysical properties that in turn will affect cloud macrophysical properties[45–47]. Incorporating aerosol concentration effects into this framework represents an important direction for future research and may further improve predictions of MLC variations. Lastly, for the radiative feedback estimated in this study, PC1 is constructed from large-scale meteorological variables. While it exhibits a strong relationship with LCF, it does not explicitly represent cloud microphysical properties (e.g., liquid water content, cloud-top height, and cloud optical thickness). Consequently, the inconsistency between low cloud changes and radiative feedback may partly reflect variations in these cloud properties.

Methods

Observational and CMIP6 model datasets

In this study, we leverage the Clouds and the Earth's Radiant Energy System (CERES) synthesis product CERES-SYN1deg-Ed4.1A to analyze the physical and radiative properties of marine low-level clouds (MLCs). Regarding the choice of the study region, MLCs' primary contributing regions are located at low latitudes, where solar insolation is much stronger. Focusing on these regions also avoids confounding influences from high-latitude storm tracks, where frontal systems and cloud formation mechanisms differ fundamentally from those in low-latitude regimes. Accordingly, this study concentrates on the mid- to low-latitude zones within 40°N–40°S, covering the period from 2010 to 2019. The observational data of low cloud fraction (LCF) used here are obtained from the CERES-MODIS joint cloud product. Based on cloud-top pressure and optical thickness, the CERES-SYN1deg-Ed4.1A product systematically classifies clouds by height, distinguishing LCF (surface-700 hPa), middle-low cloud fraction (700–500 hPa), middle-high cloud fraction (500–300 hPa), and high cloud fraction (300 hPa-tropopause). Multi-layer cloud scenarios are explicitly accounted for during cloud detection and statistics. When high clouds obscure lower clouds, the corresponding pixel is not counted toward the low cloud, thereby minimizing the direct contamination of low-cloud retrievals by overlying high clouds. As such, the CERES-observed LCF has already addressed multi-layer cloud obscuration at the data-product level.

In this study, we used two CERES-SYN1deg-Ed4.1A observational datasets with different temporal resolutions. The first dataset consists of the monthly mean LCF for 2010–2019. This dataset is used to characterize the spatial distribution of LCF and to establish the historical sensitivity of CERES-observed LCF to PC1 derived from ERA5. The second dataset consists of hourly CERES data for 2010–2019, including LCF, total cloud fraction, and the top of the atmosphere (TOA) radiative fluxes under clear-sky and all-sky conditions. These hourly data are not used directly for statistical regression, but instead serve to more precisely screen low-cloud-dominated radiative forcing at higher temporal resolution. Specifically, we retain only data where LCF constitutes more than 95% of the total cloud cover. This criterion ensures that the radiation measurements at the TOA are predominantly influenced by low clouds, thereby minimizing the contamination from other clouds[32]. To derive cloud climate feedback, our analysis focuses on radiation fluxes at the TOA under both clear-sky and all-sky conditions, with an emphasis on conditions dominated by low-level clouds. Therefore, although hourly data are involved in intermediate processing steps, all statistical analyses and feedback estimates in this study are ultimately conducted at the monthly scale, consistent with the rest of the methodology. The uncertainties related to the CERES-SYN1deg-Ed4.1A data and their potential implications are described in detail in the Supplementary Methods.

We adopt the European Centre for Medium-Range Weather Forecasts (ECMWF) for 5th generation reanalysis datasets (ERA5) to provide 40°S–40°N monthly meteorological parameters. For examining near-global scale MLCs fraction, we focused on the four key meteorological factors: SST, ω_{700}, RH_{700}, and LTS. The LTS is derived as follows[36]:

$$LTS = \theta_{700hPa} - \theta_{1000hPa} \tag{1}$$

$$\theta = T\left(\frac{1000}{P}\right)^{0.286} \tag{2}$$

where θ is the potential temperature, the subscripts "700 hPa" and "1000 hPa" indicate the corresponding pressure levels.

Determining the MLC changes is a crucial aspect of our investigation, as different future climate conditions can influence the response of low clouds to global warming, leading to varying climate feedbacks. For this analysis, we employ the CMIP6 outputs' monthly variable, focusing on historical experiments from 2010 to 2014 and future projections from 2015 to 2100 under two shared socio-economic pathways: SSP585 and SSP126. SSP585 represents a high-emission scenario with a radiative forcing of 8.5 W m^{-2} by the end of the 21st century, while SSP126 corresponds to a low-emission scenario with a radiative forcing of 2.6 W m^{-2} [48]. We applied a strict selection strategy to CMIP6 models, requiring candidate models to provide a complete and internally consistent set of key meteorological and cloud amount variables. Each model should provide SST, vertical velocity, temperature, and geopotential height at multiple vertical levels, near-surface wind speed, specific humidity, surface sensible heat flux, near-surface air temperature, and cloud fraction profiles. All these variables should be continuously available for the historical period as well as for the SSP126 and SSP585 scenarios. As a result, eight CMIP6 models satisfied all selection criteria and were included in the analysis. The selected models span a wide range of equilibrium climate sensitivity (ECS), from low (MIROC6, NorESM2-LM) to high (ACCESS-CM2, CESM2-WACCM), thereby reducing dependence on any single ECS regime and enhancing the robustness of the results. To ensure consistency across all models, the outputs from different models were re-gridded using two-dimensional cubic interpolation to a 1° × 1° resolution, aligning the data with the resolutions of CERES and ERA5. Detailed information about the eight models used is provided in Supplementary Table S1.

In CMIP6 models, low-level cloud fraction is not provided as a standalone variable, but is diagnosed from cloud fraction profiles. Following previous studies, we define low-level cloud fraction as the maximum cloud fraction at any level within the 600–1000 hPa pressure range (denoted as L), corresponding to the maximum-overlap assumption. Similarly, high-level cloud fraction is defined as the maximum cloud fraction within the 100–250 hPa range (denoted as U)[4]. The CMIP6 LCF is then calculated using the following formula:

$$LCF = \frac{L}{1 - U} \tag{3}$$

When high clouds are present within an atmospheric column, directly using the maximum low-level cloud fraction L can underestimate the potential amount of low clouds. Dividing by $1 - U$ helps to minimize the masking effect of high clouds on low clouds, and this approach has been adopted in previous studies[30]. In addition, the CERES-SYN1deg-Ed4.1A LCF is derived from satellite observations based on cloud-top pressure and optical thickness, and it only counts low clouds that are not obscured by high clouds. The formula used in this study is therefore logically consistent with the CERES processing approach, as it effectively accounts for high-cloud masking within models and maximizes the physical comparability between modeled low clouds and satellite observations.

Principal component analysis

Principal component analysis (PCA) is a mathematical technique for feature extraction that focuses the characteristics of multiple meteorological variables (e.g., SST, ω_{700}, RH_{700}, and LTS) onto principal components, thereby achieving dimensionality reduction of multidimensional data. Here, we employ PCA to extract the maximum variance direction, represented by PC1, to capture the essential meteorological conditions influencing cloud evolution. By applying PCA, we transform the complex nonlinear covariations among multiple meteorological factors into a low-dimensional linear expression, which correlates well with the evolution of LCF[32–34]. The effectiveness of PC1 in capturing and simplifying the covariation of multiple factors provides a robust description of the interrelationship between the four meteorological parameters and establishes a strong connection between meteorology and MLCs. Below is the procedure for calculating PCA:

The four meteorological variables, all with monthly data, x, are first standardized to X by subtracting their respective means ($\bar{x}$) and then being divided by their standard deviations (σ), as follows:

$$X_{i,j} = \frac{x_{i,j} - \overline{x_{i,j}}}{\sigma_i}, \tag{4}$$

where i is from 1 to 4 for the four variables, and j is from 1 to N. Here we organize the monthly data from all grid points (360 × 81) within the study area over L years (12 × L months) sequentially into a one-dimensional vector, and N is thus 360 × 81 × 12 × L. For example, N is 360 × 81 × 120 for 10 years. To focus on oceanic low clouds, all land grid points are assigned with NAN values. The bar represents the spatial and temporal average of each meteorological variable over the entire study area and period. This standardization process makes the variables dimensionless, minimizing the influence of different units across the original meteorological controlling factors. The four standardized variables are arranged into a two-dimensional matrix, as shown below:

$$X_{4\times N} = \begin{pmatrix} RH700_1 & \cdots & RH700_N \\ SST_1 & \cdots & SST_N \\ LTS_1 & \cdots & LTS_N \\ \omega700_1 & \cdots & \omega700_N \end{pmatrix}. \tag{5}$$

Solving the covariance matrix C, we have

$$C_{4\times 4} = \frac{1}{N}XX^T = \frac{1}{N}\begin{pmatrix} RH700_1 & \cdots & RH700_N \\ SST_1 & \cdots & SST_N \\ LTS_1 & \cdots & LTS_N \\ \omega700_1 & \cdots & \omega700_N \end{pmatrix}\begin{pmatrix} RH700_1 & SST_1 & LTS_1 & \omega700_1 \\ \vdots & \vdots & \vdots & \vdots \\ RH700_N & SST_N & LTS_N & \omega700_N \end{pmatrix}. \tag{6}$$

After obtaining the eigenvalues and eigenvectors of the covariance matrix, the eigenvectors are arranged in rows according to the magnitude of the corresponding eigenvalues from top to bottom, forming a matrix P,

$$P_{4\times 4} = \begin{pmatrix} mod_{11} & \cdots & mod_{14} \\ mod_{21} & \cdots & mod_{24} \\ mod_{31} & \cdots & mod_{34} \\ mod_{41} & \cdots & mod_{44} \end{pmatrix}. \tag{7}$$

Multiply the first row of matrix P in (7) by matrix X in (5) to obtain the PC1, as follows:

$$\mathrm{PC1} = PX = \begin{pmatrix} mod_{11} & \cdots & mod_{14} \end{pmatrix} \begin{pmatrix} RH700_1 & \cdots & RH700_N \\ SST_1 & \cdots & SST_N \\ LTS_1 & \cdots & LTS_N \\ \omega700_1 & \cdots & \omega700_N \end{pmatrix}, \tag{8}$$

where PC1 (i.e., PX) is one dimensional vector with N dimensionless numbers. PC1 can be rewritten as a function of latitude (φ), longitude (λ), and time (n) as PC1(φ, λ, n), where λ, φ, and n are from 1 to 360, 81, and 12 × L, respectively.

Low-level cloud fraction changes and radiative feedback

We use monthly CERES observations along with ERA5 meteorology during 2010–2019 to calculate the sensitivity of LCF to $\mathrm{PC1}_{\mathrm{ERA5}}$ at each grid. By multiplying the future $\mathrm{PC1}_{\mathrm{CMIP6}}$ changes predicted by GCM models with this sensitivity, we derive the spatial and temporal patterns of future LCF changes as shown in Eq.9. We first deseasonalize and detrend 10-year LCF monthly observations from CERES and the $\mathrm{PC1}_{\mathrm{ERA5}}$. We then perform a linear fit between these two variables to calculate the sensitivity of LCF to $\mathrm{PC1}_{\mathrm{ERA5}}$ at each grid. We determine the changes in $\mathrm{PC1}_{\mathrm{CMIP6}}$ by subtracting the mean values for the decade 2020–2029 from the mean values for 2091–2100 at each model grid and finally calculate the ensemble mean[28,31]. Finally, we multiply the historical sensitivity of LCF to $\mathrm{PC1}_{\mathrm{ERA5}}$ with the ensemble mean $\mathrm{PC1}_{\mathrm{CMIP6}}$ changes to project LCF changes at each grid, as shown in panels B (SSP126) and D (SSP585) of Fig. 3.

$$\Delta\mathrm{LCF} = \frac{\partial \mathrm{LCF}(\varphi,\lambda)}{\partial \mathrm{PC1}(\varphi,\lambda)}\,\Delta\mathrm{PC1}. \tag{9}$$

Here $\frac{\partial \mathrm{LCF}(\varphi,\lambda)}{\partial \mathrm{PC1}(\varphi,\lambda)}$ is the sensitivity through linear fitting of LCF and PC1 for each grid point during the period of 2010 to 2019. ΔPC1 is the changes in $\mathrm{PC1}_{\mathrm{CMIP6}}$. φ and λ represent the latitude and longitude within the 40°N–40°S oceanic regions, respectively.

For this study, before calculating the radiative feedback, we first use the hourly data to select time points where LCF accounts for more than 95% of the total cloud fraction, minimizing the influence of mid- and high-level clouds on TOA radiation and ensuring that the radiative forcing $R\left(\varphi,\lambda\right)$ at those hours is primarily contributed by low clouds. After this selection, the hourly radiative data are re-aggregated into monthly averages and used for subsequent calculations of MLCs' radiative feedback. The $R\,(\varphi,\lambda)$ at the TOA induced by MLCs is calculated by subtracting the corresponding screened monthly mean clear-sky radiative fluxes from the all-sky radiative fluxes at each grid point. The radiative feedback of low clouds to changes in global mean surface air temperature (T_g) can be approximated using a radiative kernel combined with the response of PC1 to global warming[8,31]:

$$\frac{\mathrm{dR}(\varphi,\lambda)}{\mathrm{dT_g}} = \frac{\partial \mathrm{R}(\varphi,\lambda)}{\partial \mathrm{PC1}(\varphi,\lambda)}\,\frac{\mathrm{dPC1}(\varphi,\lambda)}{\mathrm{dT_g}}. \tag{10}$$

Here $\frac{\partial R(\varphi,\lambda)}{\partial \mathrm{PC1}(\varphi,\lambda)}$ is the radiative kernel, representing the sensitivity of low cloud radiative forcing to changes in PC1. The monthly anomalies of R and PC1 after de-seasonalizing and detrending are linearly fitted for the CERES and ERA5 datasets during the 2010–2019, with the slope representing the PC1 kernel[6,28,31]. The term $\frac{\mathrm{dPC1}(\varphi,\lambda)}{dT_g}$ denotes the PC1 response to global warming, calculated as the ratio of the difference in the PC1 and Tg variables between the two decades of 2020-2029 and 2091-2100, respectively, for the low- and high-carbon emission scenarios[8,28,31].

Different low cloud types regime partitioning

We followed the method of refs. 30,31 and classified marine low clouds between 40°N and 40°S into four regimes—stratocumulus, trade cumulus, tropical ascent, and midlatitude regimes—based on the climatological thresholds of ω_{700} and estimated inversion strength (EIS)[49] from the 2010–2019 ERA5 observation period. We define the stratocumulus regime as grid boxes with $\omega_{700} > 15$ hPa day^{-1} and EIS > 1 K. The trade cumulus regime is defined as $\omega_{700} > 0$ hPa day^{-1} and EIS < 1 K. The tropical ascent regime includes grid boxes equatorward of 25°N and 25°S with $\omega_{700} < 0$ hPa day^{-1}. The midlatitude regime consists of grid boxes poleward of 25°N and 25°S with $\omega_{700} < 15$ hPa day^{-1} and EIS > 1 K or $\omega_{700} < 0$ hPa day^{-1}.

Feedback uncertainty calculation

Following the methodology of ref. 31, the total uncertainty in the observationally constrained feedback arises from two primary sources: (1) uncertainties in the observational estimates of $\frac{\partial R(\varphi,\lambda)}{\partial \mathrm{PC1}(\varphi,\lambda)}$, and (2) uncertainties in the model-derived changes of $\frac{\mathrm{dPC1}(\varphi,\lambda)}{dT_g}$.

The uncertainty from observations is first quantified at the grid-box level. For each grid, the 90% confidence interval of the feedback is calculated as:

$$\frac{\mathrm{dR}(\varphi,\lambda)}{\mathrm{dT_g}} \pm \mathrm{t} \times \mathrm{SE} \times \sqrt{\frac{\mathrm{N_{nom}}}{\mathrm{N_{eff}}}}|\Delta\mathrm{x}|\,. \tag{11}$$

or equivalently

$$\frac{\mathrm{dR}(\varphi,\lambda)}{\mathrm{dT_g}} \pm \delta\left(\varphi,\lambda\right). \tag{12}$$

Here, SE denotes the standard error of the regression coefficient, and $\frac{N_{nom}}{N_{eff}}$ is the ratio of the nominal to effective sample size for the monthly anomalies of $R(\varphi,\lambda)$. The term t is the critical value of the Student's t test at the 95% significance level with N_{eff} - 2 degrees of freedom. We estimate $\frac{N_{nom}}{N_{eff}}$ as $\frac{(1+r)}{(1-r)}$, where r is the lag one autocorrelation of monthly anomalies of $R(\varphi,\lambda)$. Δx represents the ensemble mean $\frac{\mathrm{dPC1}(\varphi,\lambda)}{dT_g}$ under different emission scenarios.

The confidence intervals for regime-averaged feedbacks, $\left\langle\frac{dR(\varphi,\lambda)}{dT_g}\right\rangle$, based only on uncertainty in $\frac{\partial R(\varphi,\lambda)}{\partial \mathrm{PC1}(\varphi,\lambda)}$, are calculated by propagating the error from Eq. (11) according to

$$\left\langle\frac{\mathrm{dR}(\varphi,\lambda)}{\mathrm{dT_g}}\right\rangle \pm \sqrt{\frac{\sum_{\mathrm{k=1}}^{\mathrm{N^*_{nom}}}\left(\delta_\mathrm{k}\mathrm{w_k}\right)^2}{\left(\sum_{\mathrm{k=1}}^{\mathrm{N^*_{nom}}} w_\mathrm{k}\right)^2}}\sqrt{\frac{\mathrm{N^*_{nom}}}{\mathrm{N^*_{eff}}}} \tag{13}$$

or equivalently

$$\left\langle\frac{\mathrm{dR}}{\mathrm{dT_g}}\right\rangle \pm \Delta_{\mathrm{obs}} \tag{14}$$

where δ_{k} is the uncertainty of the kth grid box, w_{k} is the cosine of latitude and $\frac{N^*_{nom}}{N^*_{eff}}$ is the ratio of the nominal to effective number of 1° × 1° grid boxes. N^*_{eff} is computed using the method of ref. 50 applied to monthly anomalies of $R(\varphi,\lambda)$ for all marine grid boxes between 40° S and 40° N.

To estimate the uncertainty arising from $\frac{\mathrm{dPC1}(\varphi,\lambda)}{dT_g}$, we first compute regime-averaged, observationally constrained feedbacks using changes in PC1 from each of the eight individual GCMs under different emission scenarios. A 90% uncertainty range is then approximated as

$$\left\langle\frac{\mathrm{dR}}{\mathrm{dT_g}}\right\rangle \pm \Delta_{\mathrm{GCMs}} \tag{15}$$

where Δ_{GCMs} is half of the 5–95 percentile range of feedback values across models under different emission scenarios, estimated via bootstrap resampling.

Finally, the total 90 % confidence interval of regime-averaged feedback under different emission scenarios is given by

$$\left\langle \frac{dR}{dT_g} \right\rangle \pm \sqrt{\Delta_{obs}^2 + \Delta_{GCMs}^2} \tag{16}$$

Data availability

Cloud, radiation, and meteorology data are from several sources. The ERA5 data on pressure levels can be found from the ECMWF Datasets center web[51] https://cds.climate.copernicus.eu/cdsapp#!/dataset/reanalysis-era5-pressure-levels?tab=form. The satellite observed cloud properties, and radiation can be obtained from the CERES website[52] https://ceres.larc.nasa.gov/data/#synoptic-toa-and-surface-fluxes-and-clouds-syn. The CMIP6 products can be available through the Earth System Grid Federation[48] https://esgf-node.llnl.gov/search/cmip6/.

Code availability

The codes used for principal component analysis and cloud feedback calculations, including all data processing procedures, are publicly available on Zenodo at: https://doi.org/10.5281/zenodo.19605450. All data processing and analysis were performed using standard MATLAB functions(version 2024b).

Received: 31 October 2025; Accepted: 17 April 2026;
Published online: 05 May 2026

References

1. Cai, W. et al. Increased ENSO sea surface temperature variability under four IPCC emission scenarios. *Nat. Clim. Chang.* **12**, 228–231 (2022).
2. Armour, K. C. et al. Sea-surface temperature pattern effects have slowed global warming and biased warming-based constraints on climate sensitivity. *Proc. Natl. Acad. Sci. USA* **121**, e2312093121 (2024).
3. Sherwood, S. C. et al. An assessment of Earth's climate sensitivity using multiple lines of evidence. *Rev. Geophys.* **58**, e2019RG000678 (2020).
4. Schiro, K. A. et al. Model spread in tropical low cloud feedback tied to overturning circulation response to warming. *Nat. Commun.* **13**, 7119 (2022).
5. Wood, R. & Hartmann, D. L. Spatial variability of liquid water path in marine low cloud: The importance of mesoscale cellular convection. *J. Clim.* **19**, 1748–1764 (2006).
6. McCoy, D. T., Eastman, R., Hartmann, D. L. & Wood, R. The change in low cloud cover in a warmed climate inferred from AIRS, MODIS, and ERA-interim. *J. Clim.* **30**, 3609–3620 (2017).
7. Bony, S. & Dufresne, J.-L. Marine boundary layer clouds at the heart of tropical cloud feedback uncertainties in climate models. *Geophys. Res. Lett.* **32**, L20806 (2005).
8. Qu, X., Hall, A., Klein, S. A. & DeAngelis, A. M. Positive tropical marine low-cloud cover feedback inferred from cloud-controlling factors. *Geophys. Res. Lett.* **42**, 7767–7775 (2015).
9. Qu, X., Hall, A., Klein, S. A. & Caldwell, P. M. On the spread of changes in marine low cloud cover in climate model simulations of the 21st century. *Clim. Dyn.* **42**, 2603–2626 (2014).
10. Randall, D. A., Coakley, J. A., Fairall, C. W., Kropfli, R. A. & Lenschow, D. H. Outlook for Research on Subtropical Marine Stratiform Clouds. *Bull. Am. Meteorol. Soc.* **65**, 1290–1301 (1984).
11. Konsta, D. et al. Low-level marine tropical clouds in six CMIP6 models are too few, too bright but also too compact and too homogeneous. *Geophys. Res. Lett.* **49**, e2021GL097593 (2022).
12. Cesana, G., Ackerman, A., Črnivec, N., Pincus, R. & Chepfer, H. An observation-based method to assess tropical stratocumulus and shallow cumulus clouds and feedbacks in CMIP6 and CMIP5 models. *Environ. Res. Commun.* **5**, 045001 (2023).
13. Zelinka, M. D., Zhou, C. & Klein, S. A. Insights from a refined decomposition of cloud feedbacks. *Geophys. Res. Lett.* **43**, 9259–9269 (2016).
14. Marvel, K., Pincus, R., Schmidt, G. A. & Miller, R. L. Internal variability and disequilibrium confound estimates of climate sensitivity from observations. *Geophys. Res. Lett.* **45**, 1595–1601 (2018).
15. Zelinka, M. D. et al. Causes of higher climate sensitivity in CMIP6 models. *Geophys. Res. Lett.* **47**, e2019GL085782 (2020).
16. Brient, F. & Schneider, T. Constraints on climate sensitivity from space-based measurements of low-cloud reflection. *J. Clim.* **29**, 5821–5835 (2016).
17. Klein, S. A. & Hall, A. Emergent constraints for cloud feedbacks. *Curr. Clim. Change Rep.* **1**, 276–287 (2015).
18. Lutsko, N. J., Popp, M., Nazarian, R. H. & Albright, A. L. Emergent constraints on regional cloud feedbacks. *Geophys. Res. Lett.* **48**, e2021GL092934 (2021).
19. Andrews, T. et al. On the effect of historical SST patterns on radiative feedback. *J. Geophys. Res. Atmos.* **127**, e2022JD036675 (2022).
20. Naud, C. M., Elsaesser, G. S. & Booth, J. F. Dominant cloud controlling factors for low-level cloud fraction: subtropical versus extratropical oceans. *Geophys. Res. Lett.* **50**, e2023GL104496 (2023).
21. Li, S. & Huang, P. An exponential-interval sampling method for evaluating equilibrium climate sensitivity via reducing internal variability noise. *Geosci. Lett.* **9**, 34 (2022).
22. Rashid, H. A. et al. Evaluation of climate variability and change in ACCESS historical simulations for CMIP6. *J. South. Hemisph. Earth Syst. Sci.* **72**, 73–92 (2022).
23. Norris, J., Hall, A., Neelin, J. D., Thackeray, C. W. & Chen, D. Evaluation of the tail of the probability distribution of daily and subdaily precipitation in CMIP6 models. *J. Clim.* **34**, 2701–2721 (2021).
24. Myers, T. A. & Norris, J. R. Reducing the uncertainty in subtropical cloud feedback. *Geophys. Res. Lett.* **43**, 2144–2148 (2016).
25. Ceppi, P., Hartmann, D. L. & Webb, M. J. Mechanisms of the negative shortwave cloud feedback in middle to high latitudes. *J. Clim.* **29**, 139–157 (2016).
26. Myers, T. A. & Norris, J. R. Observational evidence that enhanced subsidence reduces subtropical marine boundary layer cloudiness. *J. Clim.* **26**, 7507–7524 (2013).
27. Myers, T. A. & Norris, J. R. On the relationships between subtropical clouds and meteorology in observations and CMIP3 and CMIP5 models*. *J. Clim.* **28**, 2945–2967 (2015).
28. Myers, T. A., Zelinka, M. D. & Klein, S. A. Observational constraints on the cloud feedback pattern effect. *J. Clim.* **36**, 6533–6545 (2023).
29. Bitz, C. M. & Fu, Q. Arctic warming aloft is data set dependent. *Nature* **455**, E3–E4 (2008).
30. Scott, R. C. et al. Observed sensitivity of low-cloud radiative effects to meteorological perturbations over the global oceans. *J. Clim.* **33**, 7717–7734 (2020).
31. Myers, T. A. et al. Observational constraints on low cloud feedback reduce uncertainty of climate sensitivity. *Nat. Clim. Change* **11**, 501–507 (2021).
32. Li, Y. et al. Projection of low cloud variation through robust meteorological linkage and its comparison with CMIP6 models at the SACOL site. *J. Geophys. Res. Atmos.* **129**, e2023JD040668 (2024).
33. Ge, J. et al. Dust accelerates the life cycle of high clouds unveiled through strongly-constrained meteorology. *Geophys. Res. Lett.* **51**, e2024GL109998 (2024).
34. Dong, Z. et al. Comparisons of cirrus clouds and their linkages to meteorology at the SACOL and the SGP sites. *Atmos. Res.* **281**, 106467 (2023).
35. Huang, J. et al. An overview of the Semi-arid Climate and Environment Research Observatory over the Loess Plateau. *Adv. Atmos. Sci.* **25**, 906–921 (2008).

36. Klein, S. A. & Hartmann, D. L. The seasonal cycle of low stratiform clouds. *J. Clim.* **6**, 1587–1606 (1993).
37. Wu, X., Fu, Q. & Kodama, C. Response of tropical overshooting deep convection to global warming based on global cloud-resolving model simulations. *Geophys. Res. Lett.* **50**, e2023GL104210 (2023).
38. Klein, S. A. et al. Are climate model simulations of clouds improving? An evaluation using the ISCCP simulator. *J. Geophys. Res. Atmos.* **118**, 1329–1342 (2013).
39. Koshiro, T., Kawai, H. & Noda, A. T. Estimated cloud-top entrainment index explains positive low-cloud-cover feedback. *Proc. Natl. Acad. Sci. USA* **119**, e2200635119 (2022).
40. Webb, M. J., Lock, A. P. & Ogura, T. What are the main causes of positive subtropical low cloud feedbacks in climate models? *J. Adv. Model. Earth Syst.* **16**, e2023MS003716 (2024).
41. Cesana, G. V. & Del Genio, A. D. Observational constraint on cloud feedbacks suggests moderate climate sensitivity. *Nat. Clim. Change* **11**, 213–218 (2021).
42. Zhou, C., Dessler, A. E., Zelinka, M. D., Yang, P. & Wang, T. Cirrus feedback on interannual climate fluctuations. *Geophys. Res. Lett.* **41**, 9166–9173 (2014).
43. Ge, J. et al. Diurnal variations of global clouds observed from the CATS spaceborne lidar and their links to large-scale meteorological factors. *Clim. Dyn.* **57**, 2637–2651 (2021).
44. Klein, S. A., Hall, A., Norris, J. R. & Pincus, R. Low-cloud feedbacks from cloud-controlling factors: a review. *Shallow clouds, water vapor, circulation, and climate sensitivity. Space Sciences Series of ISSI,* **65**, 135–157 (2018).
45. Andersen, H. et al. Sensitivities of cloud radiative effects to large-scale meteorology and aerosols from global observations. *Atmos. Chem. Phys.* **23**, 10775–10794 (2023).
46. Wall, C. J. et al. Assessing effective radiative forcing from aerosol–cloud interactions over the global ocean. *Proc. Natl. Acad. Sci. USA* **119**, e2210481119 (2022).
47. Yuan, T. et al. Observational evidence of strong forcing from aerosol effect on low cloud coverage. *Sci. Adv.* **9**, eadh7716 (2023).
48. Eyring, V. et al. Overview of the Coupled Model Intercomparison Project Phase 6 (CMIP6) experimental design and organization. *Geosci. Model Dev.* **9**, 1937–1958 (2016).
49. Wood, R. & Bretherton, C. S. On the relationship between stratiform low cloud cover and lower-tropospheric stability. *J. Clim.* **19**, 6425–6432 (2006).
50. Bretherton, C. S., Widmann, M., Dymnikov, V. P., Wallace, J. M. & Bladé, I. The effective number of spatial degrees of freedom of a time-varying field. *J. Clim.* **12**, 1990–2009 (1999).
51. Hersbach, H. et al. The ERA5 global reanalysis. *Q. J. R. Meteorol. Soc.* **146**, 1999–2049 (2020).
52. Loeb, N. G. et al. Clouds and the Earth's radiant energy system (CERES) energy balanced and filled (EBAF) top-of-atmosphere (TOA) edition-4.0 data product. *J. Clim.* **31**, 895–918 (2018).

Acknowledgements

We thank the anonymous reviewers for their constructive comments. We thank ECMWF, CERES, and CMIP6 for making their data available. This work was supported by the Fundamental and Interdisciplinary Disciplines Breakthrough Plan of the Ministry of Education of China (Grant No. JYB2025XDXM910), and the National Natural Science Foundation of China (Grant Nos. 42427804 and 442275076).

Author contributions

J.G. and Y.L. co-designed the study. J.G. provided guidance and wrote the initial draft. Y.L. conceptualized the study, wrote the initial draft, designed the research proposal, produced the figures, conducted all data processing, and revised the manuscript. N.P. assisted with data processing. J.S. provided helpful discussions. C.Z. provided helpful discussions. J.D assisted with data processing. X.H. assisted with data processing. Z.Z. assisted with data processing. J.H. supervised the project. Q.F. provided key ideas that shaped the study and provided overall guidance.

Competing interests

The authors declare no competing interests.

Additional information

Supplementary information The online version contains supplementary material available at https://doi.org/10.1038/s43247-026-03564-2.

Correspondence and requests for materials should be addressed to Jianping Huang.

Peer review information *Communications Earth and Environment* thanks the anonymous reviewers for their contribution to the peer review of this work. Primary handling editor: ChenRui Diao. A peer review file is available.